

Kinetic energy and fluence measurements correlated with self-generated electric and magnetic fields of spatially resolved laser ablated Zr-plasma at different irradiances

Mubashir Javed

Government College University, Lahore

Shazia Bashir (✉ shaziabashir@gcu.edu.pk)

Government College University, Lahore

Mahreen Akram

Government College University, Lahore

Khaliq Mahmood

Government College University, Lahore

Rana Ayub

Government College University, Lahore

Fida Hussain

Government College University, Lahore

Nazli Fatma

Government College University, Lahore

Muqaddas Iqbal

Government College University, Lahore

Research Article

Keywords: Laser induced plasma, kinetic energy of ions, fluence of ion, fluence of electron, self-generated electric and magnetic fields

Posted Date: May 23rd, 2022

DOI: <https://doi.org/10.21203/rs.3.rs-1668544/v1>

License:  This work is licensed under a Creative Commons Attribution 4.0 International License. [Read Full License](#)

Abstract

Experimental investigations on spatially- resolved- laser-generated Zr-plasma parameters and their relationship with the Self-Generated- Electric and Magnetic- Fields (SGEMFs) at different irradiances have been performed. The Faraday Cup (FC) is employed to measure plasma species' kinetic energy (K.E) and fluence, while electric and magnetic probes are used to measure SGEMFs of Zr-plasma. The decreasing trends for evaluated values of plasma parameters and SGEMFs have been found with increasing FC axial distance from the target, whereas, increasing trends with increasing laser irradiance are observed. The kinetic energy of Zr ions increases from 1.8 keV to 11.8 keV, whereas, fluence increases from $1 \times 10^{13} \text{cm}^{-2}$ to $2 \times 10^{13} \text{cm}^{-2}$ by increasing the laser irradiance. Similarly, the electric field of Zr plasma increases from 107Vm^{-1} to 237Vm^{-1} and magnetic field increases from 235G to 590G. The generation of SGEF is attributed to charge-separation and double-layer-structure whereas, SGMF is attributed to anisotropic temperature (∇T_e) and density (∇n_e) gradients of plasma.

1. Introduction

Laser-induced plasmas (LIP) are state of the art and promising sources for generation of high energy electrons, ions, X-rays and other electromagnetic radiations [1, 2]. They have wide range of applications in the field of table top accelerators [3], material processing and thin-film deposition [4]. The LIP can be characterized by using different techniques such as Faraday Cup [5], time of flight mass spectrometry [6], Langmuir probe [7] and laser induced spectroscopy [8]. LIP is characterized by the two parameters: electron temperature (T_e) or kinetic energy of electrons / ions and electrons / ions density and fluence [1]. The evaluated parameters of plasma can be correlated with strength and magnitude of SGEMFs.

The interaction of high intensity laser beam with matter generates transient, inhomogeneous high density and high temperature plasma [9]. The investigation and spatial resolution of plasma provides the information about temperature and density gradients and charge separation which are considered to be responsible for the generation of SGEMFs [3, 10, 11]. The knowledge of SGEMFs of plasmas is also important for understanding the physical mechanisms that occur during the laser matter-interaction e.g, the formation of double layer structure [12] and plasma channels [13], charge separation [12], wake field generation, energy absorption and transportation [13].

Kelly et al. [14] evaluated the ion kinetic energy of laser induced plasma of three different materials (C, Al and Cu) by using the Faraday Cup (FC). They found the low and high kinetic energy peak in case of metallic as well as semiconductor targets. They concluded that both peaks appeared due to the ions acceleration from the double layer within the plasma. Banine et al. [15] investigated the LIP of lithium, xenon and tin as sources of extreme ultraviolet lithography (EUVL) tool that operates at a wavelength of 13.5 nm. They evaluated the tin ion plasma distribution density to be $1 \times 10^{25} \text{m}^{-3}$ for CO_2 laser operating at 10.6 μm wavelength and $1 \times 10^{27} \text{m}^{-3}$ for Nd:YAG laser operating at 1.06 μm wavelength.

Various research groups have reported their results on the SGEMF of laser induced plasma under various environmental conditions [3, 10, 11, 13, 16–25]. Kabashin et al. [3, 10] developed a probe method to investigate the structure of SGEFs of LIP of various metallic targets (Cu, Fe, W, Ti) and dielectric (Teflon) targets under air atmosphere by the pulses of different irradiances 10^9 to 10^{13}TWcm^{-2} . They observed a dipole configuration of charges for conductive target, whereas, a quadrupole configuration was observed for dielectric target. Side et al. [26] used the excimer laser ($\lambda = 248 \text{nm}$, $\tau = 25 \text{ns}$) to produce the aluminum plasma. By shifting the electric probe from 4.7 cm to 6.2 cm from the main target axis, they were able to detect temporal profiles of the electric potential. They used three laser energies of 28, 49, 56 mJ and obtained electric field of values 32, 46, 56 Vm^{-1} respectively.

Willi et al. [11] used the conducting probe to detect the SGMF of LIP of various targets (polythene, Al, Cu, W). They concluded that the detected magnetic field signal has two components which are correlated with the fast ions and thermal plasma expansion. The maximum value of SGMF is found to be of the order of 100 MG for the laser irradiance of $5 \times 10^{15} \text{GW/cm}^2$.

The motivation behind the present work is to use Faraday cups to investigate the K.E and fluence of laser-induced Zr plasma ions and electrons, as well as their relationship to SGEMFs. These investigations actually uncover the detailed spatially resolved plasma dynamics at various laser irradiances. The self-generated electric field provides pull to the ablated ions for acceleration and makes plasma more beneficial for table top accelerators. Zr is selected as a target to investigate the possibility of identifying slow and

fast ions peak based on the reported fact that thermal and prompt electron emission is possible from low Z-material. The use of low Z materials, such as Zr, to generate both slow and fast ions for wide-ranging applications as an ion source for ion implantation, thin film deposition, and table-top accelerators is an interesting aspect of the current work. Nd : YAG laser ($\lambda = 532 \text{ nm}$, $\tau = 6 \text{ ns}$) is used as a source of irradiation to produce the Zr-plasma. In order to explore the plasma spatially, the FC to target distance varies from 1 cm to 4 cm. Similarly, SGEMFs of Zr-plasma have been evaluated at the same probe-to-target distances, ranging from 1 to 4 cm. The objective of this paper is to relate charge separation, along with ∇T_e and ∇n_e with SGEMFs. The optimum combination of laser irradiance and probe to target distance has been explored to obtain the maximum value of electric and magnetic fields. The motivation also includes the Zr-plasma with measured values of ion kinetic energy, ion / electron fluence and SGEMFs that can be utilized as sources of electrons and ions and also as generators of electric and magnetic fields. No work is reported in accordance with our best knowledge in which simultaneous measurements of kinetic energy, fluence of electrons and ions, along with SGEMF of metallic plasma at various irradiance as well as various probe to target distances has been performed.

Our group has reported [27] previously the exploration of Zr plasma parameters along with SGEMF at various Ar pressures. The environment provides confinement and restricts free expansion of plasma. But the present work deals with the Zr plasma under UHV condition in which plasma expands freely. The plasma parameters and SGEMF are measured at various probe to target distance to resolve the plasma spatially. The other main difference with previous investigation of laser irradiance effects, because the laser irradiance increases mass ablation with increasing sputtering yield and consequently plasma becomes more hot after gaining enhanced collisional frequency along enhanced degree of ionization [28].

2. Experimental Setup

The target material was composed of zirconium (99.99%). The Zr-samples were ultrasonically cleaned with acetone for 20 minutes after grinding and polishing. A 532 nm Nd: YAG laser (Quantal 981C) was employed at a repetition rate of 10 Hz with pulse duration of 6 ns. All the experiments were conducted in a stainless steel vacuum chamber that was evacuated to a base pressure of 10^{-9} Torr using a turbo molecular pump (Turbo-V 81-AG) and rotatory pump. To avoid crater formation and non-uniform pitting, prepared samples were positioned on the rotating target holder with the use of a stepper motor to ensure a fresh surface for each exposure. After passing through a 50 cm focal length lens, the laser beam interacted with the target at an 90° angle to the target's surface. Using fixed laser irradiance at 90 mJ energy, the focus spot size was calculated experimentally using SEM analysis. Using the formula $A = \pi r^2$, where $r = \text{spotdiameter}/2$, the focus spot area of $1.4747 \times 10^{-3} \text{ cm}^{-2}$ was calculated. The pulse energies of 90, 110, 130, 150, 170, 190, 210 and 230 mJ correspond to laser irradiances of 10.2, 12.4, 14.7, 17, 19.2, 21.5, 23.7 and 26 GW cm^{-2} respectively.

Three different experiments were conducted.

Figure 1(a) shows a schematic of an experimental set-up for evaluating the kinetic energy and fluence of LIP of Zr ions and electrons with the help of FC using TOF measurements. Electrons and ions were captured by FC from the LIP of Zr in the first series of experiments to determine their kinetic energy and fluence. A configuration of two FCs was designed and manufactured to evaluate the kinetic energy of Zr plasma ions through TOF measurements. For this reason, a FC formed of Al having a diameter of 1.5cm as well as an area of 3.79 cm^2 was placed at an angle of 45° from the target surface normal on the vertical rod. The separation between the two FCs was kept at 6 cm. Both FCs are able to collect plasma species because the second FC2 is slightly higher than the first FC1. To capture only ions from the Zr-plasma, a negative biasing voltage of -90 V was supplied to the FC using a dc power supply (Taiwan, GPR – 6030D; GWInstrument) and an appropriate biasing circuit. A positive biasing voltage of $+90 \text{ V}$ was provided to the FC to capture only electrons from the LIP of Zr. The shape of the signal also improves significantly at -90 V as compared to lower biasing voltage. Lower biasing voltages in our work are responsible for noisy signals. The effect of increases laser irradiance becomes significantly pronounced at high biasing volts of $+90 \text{ V}$. Therefore we have selected -90 V biasing voltage for all measurement. The first FC1 was mounted at different distances of 1 cm, 2 cm, 3 cm, and 4 cm from the target surface while maintaining a fixed distance of 6cm from the other FC2 and a fixed angle of 45° from normal to the target surface. The electrons and ions signals were measured using an oscilloscope (TDS3054B, Tektronix, USA, 500MHz). A photodiode was used to receive the laser beam signal, which was then displayed on an oscilloscope.

In the second series of experiments, the SGEF of LIP of Zr was evaluated, as shown in Fig. 1(b). The electric probe was used to diagnose SGEF at four probe to target distances of 1, 2, 3, and 4 cm. The probe was placed at an angle of 45° with normal to target surface. For this purpose, a self-designed and manufactured electric probe with a length of 7.8 cm as well as a tip area of 0.95mm^2 was used. The probe was made-up of brass and was enclosed by a Teflon cylinder. The electric probe captures a particular voltage signal related to the growth of Zr-plasma charges or the potential difference among plasma voltage and the grounded Zr-target when it is positioned inside the Zr-plume. The voltage drop on the electric-probe was displayed on the oscilloscope using a filter circuit with a capacitance of 330pF and a resistance of $100\ \Omega$. The SGEF was calculated using the formula $E = \frac{V_0}{r}$ [10], where " V_0 " is the measured voltage and " r " is the distance of target from electric probe. All SGEF measurements were performed with the same irradiances, ambient conditions, and target-to-probe distances as in the first experiment.

The SGMF of LIP of Zr is determined in the third series of experiments using a (self-designed and manufactured) magnetic probe, the schematic of which is illustrated in Fig. 1(c). At probe distances of 1, 2, 3, and 4 cm from the Zr-target, the magnetic probe was positioned at an 45° angle to the target surface normal. The magnetic probe is made up of 17 turns of 1.3mm laminating copper wire which was wound on an iron core with a length of 3 cm and a probe tip area of 0.62cm^2 . The wounded copper wire was connected to the oscilloscope through a filter circuit, while another end is grounded through coaxial cable. The voltage generated on a magnetic probe is $V = NA_{mp}dB/dt$ (Faraday's Law). The SGMF was calculated using the formula $B = RCV_0/NA_{mp}$, where " N " is the number of turns in the area " A " coil and " B " is the magnetic field, based on Faraday's Law of electromagnetic induction [29]. The same irradiances, ambient conditions and target-to-probe distances as in the first and second experiments were used for all SGMF measurements.

3. Results And Discussion

3.1 Analysis of ions emitted by LIP using the FC technique

Figure 2 shows the TOF signals of ion of LIP of Zr at two selected laser irradiances (minimum irradiance of 17GWcm^{-2} and maximum irradiance of 26GWcm^{-2}) at different distances of the Faraday Cup (FC1) from the target i.e. (a) 1 cm, 17GWcm^{-2} (b) 1 cm, 26GWcm^{-2} (c) 2 cm, 17GWcm^{-2} (d) 2 cm, 26GWcm^{-2} (e) 3 cm, 17GWcm^{-2} (f) 3cm, 26GWcm^{-2} (g) 4 cm, 17GWcm^{-2} and (h) 4 cm, 26GWcm^{-2} . Two FCs were placed at a 45° angle to the normal of target surface and 6cm apart. To collect the ions, a -90 V biasing voltage was provided to both FCs.

For all distances, a single peak is found at the front Faraday Cup (FC1), while twin peaks are detected at the second Faraday Cup (FC2). The first peak is intense and sharp, indicating the production of fast ions from Zr-plasma of nanosecond duration. The second peak which appears after a delay time of microsecond from the laser signal is broad and of smaller intensity as compared to fast peak and corresponds to the production of slow ions of Zr-plasma. The appearance of fast signal of ions is due to the prompt electrons generation [5]. The hot electrons are able to escape the region of interaction without energy being transferred to the lattice. These photoelectrons are accelerated through the inverse bremsstrahlung process which is called prompt electrons. These prompt electrons cause the emission of fast ions whose energy is greater than the thermal ions [5]. It is also observed that peaks corresponding to slow ions on both Faraday Cups (FC1 and FC2) are significantly broader than the fast ions. This is due to the occurrence of a large number of thermal mechanisms, such as explosive boiling, melting, and large-scale vaporization processes. The identification of fast ion peaks for high Z material is also reported by other research groups [5, 30, 31]. However, the identification of fast and slow ions of spatially resolved laser generated plasma is not reported by any research group.

For shorter distances between the Zr-target and the first FC, such as 1 cm, 2 cm, 3 cm, and 4 cm, the fast ions peak is not found. The absence of fast peak at a closer target to detector distance is due to increase in recombination losses within the plume. As a result, the fast ions at a closer distance from the target surface are not resolved by the first FC.

Figures 2(a - h) reveal that as the distance between the FC and the target surface increases, the ionic signal amplitude reduces. It is also observed that at high irradiance of 26GWcm^{-2} , the amplitude of ionic signal (Figs. 2 (b, d, f and h)) is slightly higher than the signals obtained at laser irradiance at 17GWcm^{-2} (Figs. 2 (a, c, e and g)). These graphs also show that with increasing laser irradiance the time delay between two signals decreases significantly. The enhancement in ionic signal with increasing laser

irradiance represents enhanced ablation rate, whereas, decrease in time delay represents enhancement in velocity of ejected species due to the more energy deposition. From FC1, the time delay between the peak of the laser signal and the peak of the ion signal is 1.02 μ s. The time delay between the signals of fast and slow ion in comparison to the laser signal on FC2 is 25.4 ns and 1.34 μ s, respectively.

The K.E of LIP of Zr ions is evaluated by using TOF measurements, which is determined by using the formula below [32].

$$\text{Kinetic Energy} = \frac{1}{2}M\nu^2 \quad (1)$$

where "M" is the atomic mass of Zr ion and " ν " Zr ions velocity which is calculated by using the formula.

$$\nu = \frac{s}{\tau}$$

2

$$\nu = \frac{\text{DistancebetweenthetwoFCs}}{\text{TimedelaybetweentheionsignalsoftwoFCs}}$$

$$s = 6\text{cm (constantdistancebetweentwoFCs)}$$

$$\tau = \text{Timedelaysthatvariesfrom680nsto900nsarematchedinFig. 2(a - h)}$$

The following equation is used to evaluated the Zr ion fluence [2].

$$n_i = \frac{V \times t}{qAR}$$

3

where "V" represents the amplitude of the ion voltage signals received on FC1 (seen in Figs. 2(a-h)), "t" is the "FWHM" of the ion voltage signal acquired on FC1, "q" represents the ion charge's magnitude, "A" is the FC aperture area, and the load resistance over which the ion pulse output is obtained is denoted by "R."

3.1.1 Effect of laser irradiance on kinetic energy of Zr plasma ions

Figure 3 shows the kinetic energy of Zr-plasma as the laser irradiation increases at various distances of 1, 2, 3, and 4 cm of FC from the surface of the target. A maximum kinetic energy of Zr ions was measured at a distance of 1 cm from the target surface, ranging from 1.8 keV to 11.8 keV while at 4 cm from the target surface the minimum K.E of the Zr ions was measured from 0.7 keV to 3.9 keV, with the increase in the laser irradiance from 10.2 to 26 GWcm^{-2} for each distance. The kinetic energy of Zr ions increases as the laser irradiance increases, which are due to increased energy deposition, collisions between ions and other plasma species and thermal vaporization [33]. It is also noticed that the kinetic energy of Zr ions decreases as the distance from the FC to the surface of target increases. It is due to plume expansion because Zr ions take more time to reach the FC and lose their kinetic energy at longer distances.

3.1.2 Effect of laser irradiance on Zr-plasma ion fluence

Figure 4 shows the ion fluence of Zr-plasmas, with increasing laser irradiances at various distances of 1, 2, 3, and 4 cm of FC from Zr target. The fluence of Zr ions increases as laser irradiance increases, due to a greater ablation rate and higher energy deposition [28]. With increase in irradiance both photothermal and photophysical processes become more pronounced and consequently more melting, vaporization and ionization occur along with enhanced collisional frequency [34]. The Zr ion fluence decreases with increase in FC to target distances which is attributed to the conical shaped plume expansion. Due to which the number of ions per unit area at greater distances is significantly reduced.

3.2 Analysis of electron emission of LIP by using FC technique

Figure 5 illustrates simple TOF signals of electrons of Zr-plasma at two different laser irradiances and at different Faraday Cup (FC1) distances from the target, i.e. (a) 1 cm, 17 GWcm^{-2} (b) 1 cm, 26 GWcm^{-2} (c) 2 cm, 17 GWcm^{-2} (d) 2 cm, 26 GWcm^{-2} (e) 3 cm, 17 GWcm^{-2} (f) 3cm, 26 GWcm^{-2} (g) 4 cm, 17 GWcm^{-2} and (h) 4 cm, 26 GWcm^{-2} . Two FCs were placed at a 45° angle with a fixed distance of 6cm between them. The electrons were collected using a biasing voltage of +90 V that was also sufficient to oppose the ions.

The broadening and amplitude of such electronic signals received from the FC are found to be significantly influenced by laser irradiance as well as the distance from the surface of target. The broadening of the electron peak relates to the electron emissions from the plasma's core [31]. The amplitude of signal voltage increases with increasing the laser irradiance and decreases with increasing the FC to target distance. The fluence of the electrons decreases with increasing the target surface distance as shown in the Fig. 6 which is attributed to the plume expansion, cooling, recombination and collisional losses [31].

The slightly higher fluence of electrons than ions is attributed to the lighter mass of electrons as compared to massive ions. Due to double layer structures, more electrons travel forward because of their lower weight and enhanced collisions of these electrons generate higher number of electrons than ions [14]. The electrons with certain energies are collected at particular distance of FC from target is greater than that of ions. The FWHM of electrons signal varies from $6.25 \mu\text{s}$ to $11.4 \mu\text{s}$ and which are significantly higher than FWHM of ions signal whose variation is from $4.36 \mu\text{s}$ to $5.8 \mu\text{s}$ at a distance of 1cm from FC to target.

3.3 SGEF of Zr-plasma under vacuum

Figure 7 illustrate the temporal profiles of electric probe (red trace) of Zr-plasma and the laser pulse (black trace) at two selected laser irradiances (lowest irradiance of 17 GWcm^{-2} and highest irradiance of 26 GWcm^{-2}) at different electric probe distances from the target i.e (a) 1 cm, 17 GWcm^{-2} (b) 1 cm, 26 GWcm^{-2} (c) 2 cm, 17 GWcm^{-2} (d) 2 cm, 26 GWcm^{-2} (e) 3 cm, 17 GWcm^{-2} (f) 3cm, 26 GWcm^{-2} (g) 4 cm, 17 GWcm^{-2} and (h) 4 cm, 26 GWcm^{-2} . The amplitude of the SGEF signal reduces as the distance of probe to target increases from 1 cm to 4 cm. This trend is observed at all irradiances. However, with increasing laser irradiance from 10.2 GWcm^{-2} to 26 GWcm^{-2} the increase in electric field signal is observed from 1 V to 2.5 V at the probe to target distance of 1 cm. This trend holds at all probes to target distances. The time duration from the start of the pulse of laser to the start of the SGEF signal is called the arrival time of the SGEF signal. When the laser irradiance increases, the arrival time of the SGEF signal reduces from 4 ns to 1.4 ns at the distance of the probe to the target of 1 cm. The leading edge of the laser pulse evaporates the surface layer of the target which generates the electric field at the beginning of laser pulse. The trailing edge passes through the LIP generated by the leading edge. The electric field of electromagnetic radiation further accelerates the charge species of plasma asymmetrically which is responsible for charge separation which produces the electron pressure gradients at the front of optical detonation waves. This asymmetry is disappeared by the end of laser pulse which does not creates the electric field after the completion of laser pulse [16]. In the present case the oxide layer on the Zr surface can be easily formed due to its reactivity towards the oxygen which leads to quadrupole distribution of laser induced Zr plasma. For the confirmation of oxide layer on Zr or Zirconium Oxide (ZrO_2), we have analyzed our unexposed and laser irradiated Zr target by XRD analysis. The oxide formation on Zr is confirmed by the XRD patterns shown in Fig. 8. Figure 8 represents the XRD patterns of unexposed and laser irradiated Zr for two laser irradiances of 17 GWcm^{-2} and 26 GWcm^{-2} . For unexposed and laser treated Zr targets, various diffraction peaks have been observed at different angles. For unexposed and laser-irradiated Zr specimens, the peaks are identified which correspond to phases of ZrO_2 at an angle of 29.8° and 101.9° with diffraction planes (101) and (321), respectively. The peaks of Zr and ZrO_2 are well matched with the card numbers [00-005-0665] and [00-042-1164] respectively. It is confirmed that oxides are present in both unexposed and laser irradiated samples. The conductivity of the upper layer of the target surface has been reported to be a key factor in the structure of the plasma-induced electric field. Due to its dielectric nature, a thin coating of oxide on a conducting target can cause a quadrupole plasma charge distribution [3]. The formation of two oppositely directed dipoles at the leading and trailing plasma fronts, resulting in a bipolar signal profile, is accompanied by the formation of LIP over a dielectric [10]. For the shorter wavelength lasers, the plasma splits in two parts which is called dual core plasma. One core is located closer to the target surface, while the other is located further away. The dipoles in this dual core plasma are in opposite directions and each has its own SGEF [21]. The similar quadrupole distribution for dielectric target having oxide layer is reported by Kabashin et al. [3].

3.3.1 Dependence of SGEF on the laser irradiance and probe to target distance

The evaluated values of the SGEF with increasing the laser irradiances for various probe to target distances of 1, 2, 3 and 4cm is shown in Fig. 9. It is observed from this graph that electric field value reduces with increasing the probe to target distance. For the given irradiance regime from 10.2 to 26 GWcm⁻², the electric field values varies from 107 to 237 Vm⁻¹, 40 to 91.5 Vm⁻¹, 23.8 to 65.7 Vm⁻¹ and 17.2 to 40.8 Vm⁻¹ at a distances of 1, 2, 3 and 4 cm respectively.

The SGEF increases with increasing the laser irradiance. As the irradiance increases, the ablation rate also increases due to enhanced energy deposition which is responsible for more electrons and ions generation. The fast moving electrons move more forward than ions and cause enhancement of charge separation at higher laser irradiances. The electric dipole moment is higher. As a result, the SGEF increases with increasing the laser irradiance. From Fig. 9, it is observed that due to adiabatic expansion of plasma, the SGEF decreases as the probe to target distance increases. It is observed that SGEF disappears after the termination of laser pulse because the asymmetric behavior of ∇n_e and ∇T_e at front of the optical detonation waves vanishes after the termination of the laser pulse [16], i.e, the SGEF which is generated due to the charge separation (double layer) is localized in the plasma and the electric field decreases with the increase in probe to target distance [16].

3.4 SGMF of Zr-plasma under vacuum

Figures 10 illustrate the temporal profiles of the magnetic probe signal (red trace) of Zr-plasma and the laser pulse (black trace) at two selected laser irradiances (lowest irradiance of 17 GWcm⁻² and highest irradiance of 26 GWcm⁻²) at different magnetic probe distances from the target i.e. (a) 1 cm, 17 GWcm⁻² (b) 1 cm, 26 GWcm⁻² (c) 2 cm, 17 GWcm⁻² (d) 2 cm, 26 GWcm⁻² (e) 3 cm, 17 GWcm⁻² (f) 3cm, 26 GWcm⁻² (g) 4 cm, 17 GWcm⁻² and (h) 4 cm, 26 GWcm⁻². It is observed that the amplitude of the SGMF signal decreases when the probe is moved from 1 cm to 4 cm away from the target. However, with increasing laser irradiance from 10.2 GWcm⁻² to 26 GWcm⁻² the increase in magnetic field signal is observed from 500 mV to 1.2 V at the probe to target distance of 1 cm. This trend holds at all probes to target distances. The magnetic field signal exhibits a bipolar nature in which the arrival time for positive peak is 6 ns and for negative peak are 27 ns. The total duration of the magnetic field signals are 44 ns. The self-generated magnetic field changes its direction at the leading and trailing front of the plume due to the electric quadrupole structure of plume. It is related to the opposition current in the laser induced plasma. The dual core plasma consists of the dipoles which are in the opposite directions. Inside both plasma cores, the positive current flows in the opposite direction in each ionizing front [29]. In the Figs. 10(a – h) the positive trace shows the positive current of dipole is becoming in the front of the plume, whereas, the negative trace in Figs. 10(a – h) indicate that the negative current of dipole is formed at the rear part of the plume. Both the kind of currents generate their own opposite magnetic fields which are concentric to the laser axis and indicate the quadrupole distribution of charges [29].

3.4.1 Dependence of SGMF on the laser irradiance and probe to target distance

The calculated values of the SGMF with increasing the laser irradiances for the different probe to target distances of 1, 2, 3 and 4cm is shown in Fig. 11. The SGMF increases from the 235 G to 590 G at a distance of 1 cm, from 195 G to 415 G at a distance of 2 cm, from 120 G to 355 G at a distance of 3 cm and from 70 G to 260 G at a distance of 4 cm increasing the laser irradiances from 10.2 to 26 GWcm⁻². There is a linear increase in the SGMF with increasing the laser irradiance due to an increase in the density of emitted charged species after greater energy deposition. The hot electron gain more energy form the source [11]. The most of the laser pulse energy converts to the kinetic energy of ions and electrons and remaining part of the energy goes to their magnetic field energy.

Due to the shielding effect, the laser absorption efficiency in plasma as compared to target increases as the laser irradiance increases. The component of electric field $E_d = 2E_L \sin\theta$ of incoming laser pulse is normal to the target surface. This electric field accelerates the charges species in the LIP. Therefore, an increase in the laser irradiance the electric field strength of the laser increases which in turns the generation and acceleration of ions / electrons and SGMF of LIP increases [35]. Figure 11 shows that the SGMF is reduced by increasing the distance of probe from the target. This is because the source of the SGMF is near the target

and moving away from the magnetic field line, the magnetic field becomes weaker [19, 24]. In the Figs. 9 (a – h) the very noticeable feature is the peak arrival time which is reduced by reducing the probe to target distance. Since the propagation of magnetic field front and the laser produced expanding plasma front are moving with same velocity.

The SGMF signal is delayed because it moves too far from the target to magnetic probe [19]. Therefore both the amplitude of the signals and SGMF decrease at longer probe to target distance. This result shows that the SGMF expands radially according to the Biot-Savart relation [20].

The laser-induced plasma can produce self-generated magnetic and electric fields. The generation of these fields can be caused by a number of factors, including the abundance of charged particles, strong electric currents, the laser wake field, the ponderomotive, and Coulomb forces.[36] Laser-induced self-generated magnetic fields have a significant impact on plasma conditions and dynamical evolution in terms of inertial confinement fusion, fast electron transport, and heat conduction in plasmas [37]. Among the various mechanisms proposed for their generation, among the various mechanisms proposed for their generation, four important physical mechanisms are (i) charge separation between fast moving electrons and slow moving ions. three important physical mechanisms are (ii) non-parallel temperature and density gradients (The Biermann battery effect) [36], (iii) the current of fast electrons produced by laser target interaction can lead to axial magnetic field generation [38], and (iv) the huge radiation pressure associated with laser pulse (Ponderomotive force) is a source of azimuthal magnetic fields in the critical density region [39]. The first theory of charge separation or charge imbalance is considered in the present investigations as a most favorable mechanism for generation of electric field in the plasma.

Figure 12 shows the separation of charge with double layer structure among fast and slow moving Zr-electrons, as well as fast and slow moving ions of Zr with ambipolar acceleration, which represents quadrupole distribution, during the LIP of Zr. In the LIP, during plume expansion, plasma species convert thermal energy into translational energy [40]. The kinetic energy and the fluence of ions and electrons are important parameter that describe the expansion of laser induced plasma dynamics [31]. The ejection process of ions and electrons occurs during the initial stage of laser matter interaction. As the plasma plume travels perpendicular to the target's surface, pressure gradients are formed. The plume expands according to the Maxwell distribution due to the large number of collision between the plasma species within the Knudsen layer [41]. The plasma plume expands because of the adiabatic process after laser pulse termination [42]. The hydrodynamic and electrostatic forces accelerate the ions and electrons in the forward direction. This forward peaking is responsible for higher the kinetic energy of charge species than the neutral species in the LIP. The Inverse Bremsstrahlung (IB) absorption heats the electrons, which then transfer their absorbed energy to the ions through electron-ions collisions in the electrostatic mode [33]. The thermalization time $10^{-10} - 10^{-11}$ s of electrons-ions is smaller than the duration of laser pulse (6×10^{-9} s) [5, 12]. Therefore during the early stage of laser matter interaction, the electrons and ions attain the same thermal temperature. Electrons achieve the highest thermal velocity, because of small size and lightest among the plasma species and they travel faster than ions. The ions lag behind which prevents the complete escaping of the electrons and the self-electrostatic field is developed which is called self-generated electric field. This SGEF is directly proportional to the K.E of the ions and the charge state. The LIP which is created by the nano second laser displays the thermal nature. The electrons obtain energy from the IB process, reheat the LIP at a fixed distance, which sustains the acceleration process [5]. The pressure gradients are caused by electrons density gradient being ejected from normal to the target. The ions gain kinetic energy by this process of acceleration caused by the separation of charges. The decrease in average kinetic energy of ions is responsible for the spatial distribution of acceleration potential [43]. Whereas, in the electrostatic model, the ions are accelerated, which is attributed to the ambipolar electric field (double layer) effect in the laser induced plasma. The double layer is formed by the ejection of energetic electrons, which is caused by the three body recombination and IB absorption process [44]. The charge imbalance generated in the LIP is responsible for the escaping process of energetic electrons, which also causes ions to accelerate. The acceleration of ejected species of plasma is maintained by the double layer potential difference [9]. The expansion of LIP is axisymmetric, so the ∇T_e and ∇n_e are non-parallel in the direction of expanding plasma. This combination of non-parallel ∇T_e and ∇n_e generates the SGMF in the LIP [13]. During the laser heating of the plasma, the ∇T_e is directed along the axis of the target surface and ∇n_e is directed along the laser axis [45]. These pressure gradients decrease as the probe moves away from the surface of target [18]. The overall mechanisms are explained in Fig. 12.

The SGEF can also be estimated by the following relation [46].

$$E_f = \frac{\nabla P_e}{n_e e} = \frac{\nabla T_e}{e} + T_e \frac{\nabla n_e}{n_e}$$

4

where “e” is the charge on electron and “ $\nabla P_e = n_e T_e$ ”, is the pressure of plasma or electron pressure (T_e in eV). At a laser irradiance of 26 GW cm^{-2} and target-to-probe distance of 1 cm, the self-generated electric field obtained from Eq. (4) is, $E_f \tilde{3}.97 \times 10^3 \text{ V/m}$ with the temperature gradient of $\nabla T_e \tilde{3}.9678 \text{ KeV}$ and density gradient of $\nabla n_e \tilde{8}.97 \times 10^{11} \text{ cm}^{-2}$. The electrons and ions densities along the axially resolved Zr plasma provide information about temperature and density gradients of electrons and ions in axial direction and charge separation, which are supposed to be responsible for the generation of SGEMFs [47]. Fast electrons leave the plasma plume much earlier than ions due to the higher mobility of electrons than ions. Some electrons are prevented from escaping the plasma due to the space-charge separation between the fast electrons and the ions that are lagging behind, leading to the formation of a self-generated electric field in the expanding plasma-vacuum boundary [48]. Table 1 indicates the individual ion density gradients, electron density gradients, and ions-electrons density gradients of Zr plasma, with increasing laser irradiances at various distances of 1, 2, 3, and 4 cm of FC from the Zr target. The values of electron density gradients from 1 cm to 2 cm were used to estimate the electric field from Eq. (4). The SGEF depends upon the pressure gradients of plasma which in turn are dependent upon ∇T_e and ∇n_e . The estimated values of electric field from Eq. (4) with directly measured values of electric field by electric probe are plotted in Fig. 13. These values are in good agreement with each other, which confirm that our experimental measured values of electric field by electric probe are accurate. The estimated electric field values from Eq. (4) and the directly measured electric field values by electric probe are presented in Fig. 13 and indicate significant differences. The density and temperature gradients are measured by the FC, whereas the self-generated electric field is measured by the electric probe. The difference in area between the FC (3.79 cm^2) and the electric probe (tip area 0.95 mm^2) is responsible for the difference in estimated electric field values and directly measured electric field values by an electric probe. The adiabatic plume expansion, cooling, condensation, recombination, and collisional losses are another possible reason for the significantly higher analytically estimated electric field values than measured electric field [31].

Table 1

The ion density and electron density gradients of Zr plasma, with increasing laser irradiances at various distances of 1, 2, 3, and 4 cm of FC from Zr target.

Irradiances ($GWcm^{-2}$)	lons density gradient	lons density gradient	lons density gradient	Electrons density gradient	Electrons density gradient	Electrons density gradient	Charge separation or lons and electrons	Charge separation or lons and electrons	Charge separation or lons and electrons
	cm^{-2}	cm^{-2}	cm^{-2}	cm^{-2}	cm^{-2}	cm^{-2}	density gradient	density gradient	density gradient
	(1 cm to 2 cm)	(2 cm to 3 cm)	(3 cm to 4 cm)	(1 cm to 2 cm)	(2 cm to 3 cm)	(3 cm to 4 cm)	cm^{-2} (1 cm to 2 cm)	cm^{-2} (2 cm to 3 cm)	cm^{-2} (3 cm to 4 cm)
10.2	9.41E+11	1.01E+12	1.70E+12	6.97E+11	1.08E+12	2.38E+11	2.44E+11	7.00E+10	1.46E+12
12.4	9.40E+11	3.13E+11	1.69E+12	1.79E+11	2.03E+12	1.57E+11	7.61E+11	1.72E+12	1.53E+12
14.7	3.98E+11	2.28E+11	2.34E+12	2.53E+10	2.84E+11	7.70E+11	4.23E+11	5.12E+11	1.57E+12
17	2.05E+11	8.85E+11	2.48E+12	1.72E+11	1.43E+11	6.43E+11	3.30E+10	1.03E+12	1.84E+12
19.2	4.06E+10	8.96E+11	1.80E+12	7.16E+10	9.48E+10	1.14E+12	3.10E+10	8.01E+11	6.60E+11
21.5	9.33E+10	4.18E+11	2.23E+12	1.59E+10	4.27E+11	2.93E+12	7.74E+10	9.00E+09	7.00E+11
23.7	1.44E+11	7.79E+11	3.36E+12	5.26E+11	6.55E+11	2.22E+12	3.82E+11	1.24E+11	1.14E+12
26	3.70E+11	1.50E+11	9.05E+11	8.97E+11	3.63E+11	2.31E+12	5.27E+11	2.13E+11	1.41E+12

The double layer structure of the plasma is confirmed by both measurement i.e. time-of-flight measurement of ions by faraday cup and electric field by electric probe.

4. Conclusions

The kinetic energy and fluence of laser-generated Zr plasma ions and electrons have been explored by the Faraday cup technique. The plasma is generated by irradiating the Zr-target with a Nd: YAG laser at various irradiances ranging from 10.2 $GWcm^{-2}$ to 26 $GWcm^{-2}$. It is found that with increasing laser irradiance, both fluence and K.E of Zr-ions / electrons show an increasing trend. Electrons, on the other hand, have a greater fluence than ions. The significant decrease in the kinetic energy and fluence of ions was observed with increasing the distance of FC detector from target. Studies of TOF ion emission in Zr plasma revealed the twin peaks of ions signals which related to the presence of two forms of ions: fast ions and slow ions, but only at a greater distance from the surface of the target.

The effect of laser irradiance on the SGEMF is also explored. It is found that both electric and magnetic field increase with increasing the laser irradiance and show a decreasing trend with increasing probe to target distance.

The SGEF is generated by charge separation, and the quadrupole is verified, which agrees with the twin peak identifications of ions by FC. The estimated values of SGEF confirm the magnetic field origination due to pressure gradients as well as ion and electron currents from the target plasma and charge separation of charges in the expanding LIP of plasma.

The estimated values of electric field from plasma temperature and density gradient are in good agreement with the measured values of electric field by electric probe. This plasma may be used as a source of electrons, ions and magnetic and electric fields for different applications for material processing, table top accelerators and magnetic confinement, as well as thin film deposition.

Declarations

Author's Contributions:

All authors contributed in this work. "Mubashir Javed" performed the experiment and wrote the paper's manuscript. The entire project was supervised by "Shazia Bashir." She was given the experimental work idea and helped in the writing of the paper. The whole experimental work was guided by "Mahreen Akram.". "Abdul khaliq" was in charge of running the laser and directing the experiment.

"Rana Ayub" helped in the measurement of Kinetic energy of ions and contributed to the Faraday cup measurements. "Fida Hussain" contributed to the self-generating electric and magnetic field experiment. "Nazli Fatma" participated with the Faraday cup experiment and contributed to the paper's writing. "Muqaddas Iqbal" participated with the magnetic field experiment and contributed to the paper's writing.

Conflict of Interest:

On the behalf of all authors I hereby declare no personal interest and disclose that there is no potential competing interest or non-financial interests.

Data availability statement:

The data that supports the findings of this study are available from the corresponding author upon reasonable request.

Funding:

No funding is available for completion of this project

Ethical Statement:

The data fulfils all ethical guidelines. No biological samples have been used for measurements

References

1. K. Bhatti, M. Khaleeq-ur-Rahman, M. Rafique, K. Chaudhary, A. Latif, *vacuum* **84**, 980-985 (2010)
2. M.B. Tahir, M. Rafique, M.S. Rafique, T.I. Awan, G. Nabi, *Indian J. Pure Appl. Phys.* **55**, 145-154 (2017)
3. A. Kabashin, P. Nikitin, W. Marine, M. Sentis, *Appl. Phys. Lett.* **73**, 25-27 (1998)
4. L. Torrisi, A. Borrielli, F. Caridi, D. Margarone, S. Gammino, N. Gambino, *Proceedings of the 35th EPS Conference on Plasma Physics, Hersonissos Greece 9-13 (2008)*
5. A.M. Elsieid, P.K. Diwakar, M. Polek, A. Hassanein, *J. Appl. Phys.* **120**, 173104 (2016)
6. S. Tudisco, D. Mascali, N. Gambino, A. Anzalone, S. Gammino, F. Musumeci, A. Scordino, A. Spitaleri, *Nucl. Instrum. Methods Phys. Res* **653**, 47-51 (2011)
7. A. Dogar, B. Ilyas, S. Ullah, A. Nadeem, A. Qayyum, *IEEE Trans Plasma Sci IEEE Nucl Plasma Sci Soc.* **39**, 897-900 (2011)
8. S. Khan, S. Bashir, A. Hayat, M. Khaleeq-ur-Rahman, Faizan-ul-Haq, *Phys. Plasmas* **20**, 073104 (2013)
9. L. Romagnani, M. Borghesi, C. Cecchetti, S. Kar, P. Antici, P. Audebert, S. Bandhoupadjay, F. Ceccherini, T. Cowan, J. Fuchs, *Laser Part.* **26**, 241 (2008)
10. A.V. Kabashin, P.I. Nikitin, W. Marine, M. Sentis, *Quantum Electron.* **28**, 24 (1998)
11. O. Willi, A. Raven, P. Rumsby, *Phys. Lett. A* **71**, 435-437 (1979)
12. X. Wang, S. Zhang, X. Cheng, E. Zhu, W. Hang, B. Huang, *Spectrochim. Acta B* **99**, 101-114 (2014)
13. A. Abudurexiti, *6th International Symposium on Advanced Optical Manufacturing and Testing Technologies: Advanced Optical Manufacturing Technologies* **8416**, 84162K (2012)
14. T. Kelly, T. Butler, N. Walsh, P. Hayden, J. Costello, *Phys. Plasmas* **22**, 123112 (2015)
15. V.Y. Banine, K. Koshelev, G. Swinkels, *J. Phys. D J PHYS D APPL PHYS* **44**, 253001 (2011)
16. V. Ageev, A. Barchukov, V. Konov, T. Murina, P. Nikitin, A. Prokhorov, A. Silenok, N. Chapliev, *Zh. Eksp. Teor. Fiz* **76**, 158-163 (1979)

17. A. Barchukov, V. Konov, P. Nikitin, A. Prokhorov, Phys. - JETP **51**, 482-486 (1980)
18. R. Bird, L. McKee, F. Schwirzke, A. Cooper, Phys. Rev. A **7**, 1328 (1973)
19. M. Drouet, R. Bolton, P. Kieffer, G. Saint-Hilaire, Z. Szili, H. Pepin, B. Grek, J. Appl. Phys. **48**, 2525-2530 (1977)
20. D.F. Edwards, V. Korobkin, S. Motilyov, R. Serov, Phys. Rev. A **16**, 2437 (1977)
21. J.M.P. Fuentes, C. Sanchez-Ake, F.O. Bredice, M. Villagrán-Muniz, J. Phys. D **46**, 495202 (2013)
22. A.V. Kabashin, P.I. Nikitin, Quantum Electron. **27**, 536 (1997)
23. Y. Lu, M. Hong, J. Appl. Phys. **86**, 2812-2817 (1999)
24. R. Serov, M. Richardson, Appl. Phys. Lett. **28**, 115-118 (1976)
25. A. Thein, Y. Kitagawa, Y. Yamada, R. Takahashi, I. Tsuda, M. Yokoyama, Jpn. J. Appl. Phys **17**, 245 (1978)
26. D. Delle Side, E. Giuffreda, V. Nassisi, Nucl. Instrum. Methods Phys. Res., B **406**, 185-187 (2017)
27. M. Javed, S. Bashir, M. Akram, K. Mahmood, R. Ayub, F. Hussain, N. Fatma, M. Iqbal, Optik **246**, 167790 (2021)
28. S.M.A. Sarfraz, S. Bashir, K. Mahmood, A. Khaliq, R. Rizvi, JOSA B **36**, 1945-1957 (2019)
29. J.M. Paulin-Fuentes, C. Sánchez-Aké, F.O. Bredice, M. Villagrán-Muniz, J. Phys. D **48**, 285204 (2015)
30. J. Prokūpek, J. Kaufman, D. Margarone, M. Krūs, A. Velyhan, J. Krása, T. Burris-Mog, S. Busold, O. Deppert, T. Cowan, Rev. Sci. Instrum. **85**, 013302 (2014)
31. N. Farid, S. Harilal, H. Ding, A. Hassanein, Phys. Plasmas **20**, 073114 (2013)
32. S.R. Mohanty, H. Bhuyan, N.K. Neog, R.K. Rout, E. Hotta, Jpn. J. Appl. Phys **44**, 5199 (2005)
33. W. Dementroder, W. Jantz, J. Plasma Phys. **12**, 691 (1970)
34. C. Walters, R. Barnes, R. Beverly III, J. Appl. Phys. **49**, 2937-2949 (1978)
35. L. Huang, H. Takabe, T. Cowan, High Power Laser Sci. Eng. **7**, (2019)
36. J. Stamper, K. Papadopoulos, R. Sudan, S. Dean, E. McLean, J. Dawson, Phys. Rev. Lett **26**, 1012 (1971)
37. W. Farmer, J. Koning, D. Strozzi, D. Hinkel, L. Berzak Hopkins, O. Jones, M. Rosen, Physics of Plasmas **24**, 052703 (2017)
38. E. Clark, K. Krushelnick, J. Davies, M. Zepf, M. Tatarakis, F. Beg, A. Machacek, P. Norreys, M. Santala, I. Watts, Physical Review Letters **84**, 670 (2000)
39. R. Sudan, Physical review letters **70**, 3075 (1993)
40. S. Amoruso, M. Armenante, V. Berardi, R. Bruzzese, N. Spinelli, Appl. Phys. A **65**, 265-271 (1997)
41. S. Amoruso, R. Bruzzese, N. Spinelli, R. Velotta, J PHYS B-AT MOL OPT **32**, R131 (1999)
42. S. Anisimov, B. Luk'Yanchuk, A. Luches, Appl. Surf. Sci **96**, 24-32 (1996)
43. A. O'connor, O. Morris, E. Sokell, J. Appl. Phys. **109**, 073301 (2011)
44. I.R. SKOY, Laser Part. **14**, 369-384 (1996)
45. L. McKee, R. Bird, F. Schwirzke, Phys. Rev. A **9**, 1305 (1974)
46. A. Prokhorov, V. Sidorinn, V. Chudnenko, JETP Lett **26**, (1977)
47. S. Baliyan, M. Rafat, A. Panwar, V. Sajal, C. Ryu, Optik **172**, 437-442 (2018)
48. M.H.A. Shaim, H.E. Elsayed-Ali, Journal of Applied Physics **122**, 203301 (2017)

Figures

Figure 1 (a)

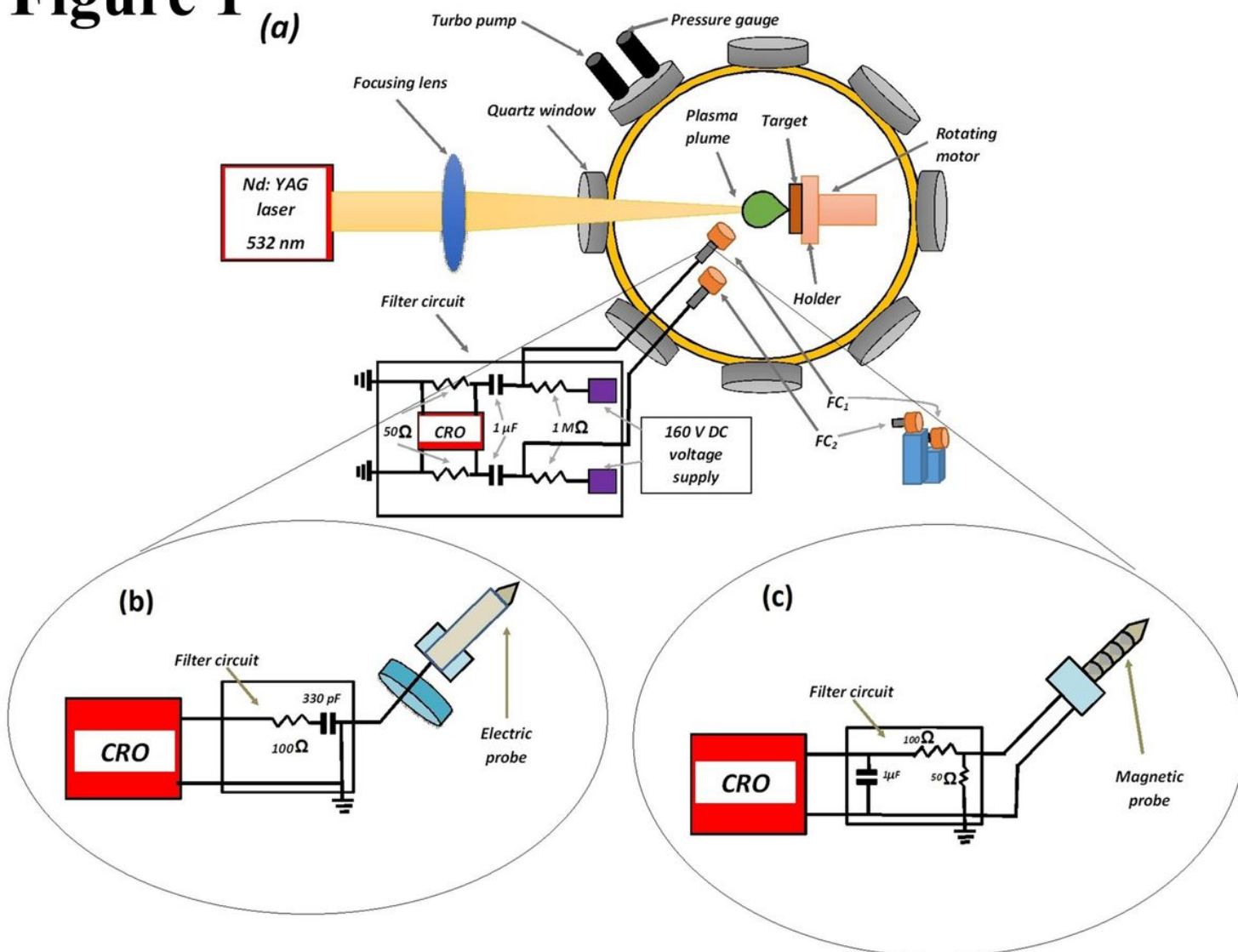


Figure 1

Schematic of experimental set-up for the (a) calculating the K.E and fluence of Zr plasma ions and electrons by using Faraday Cup using time of flight measurements (b) self-generated electric field measurements and (c) self-generated magnetic field measurements of the laser induced Zr-plasma.

Figure 2

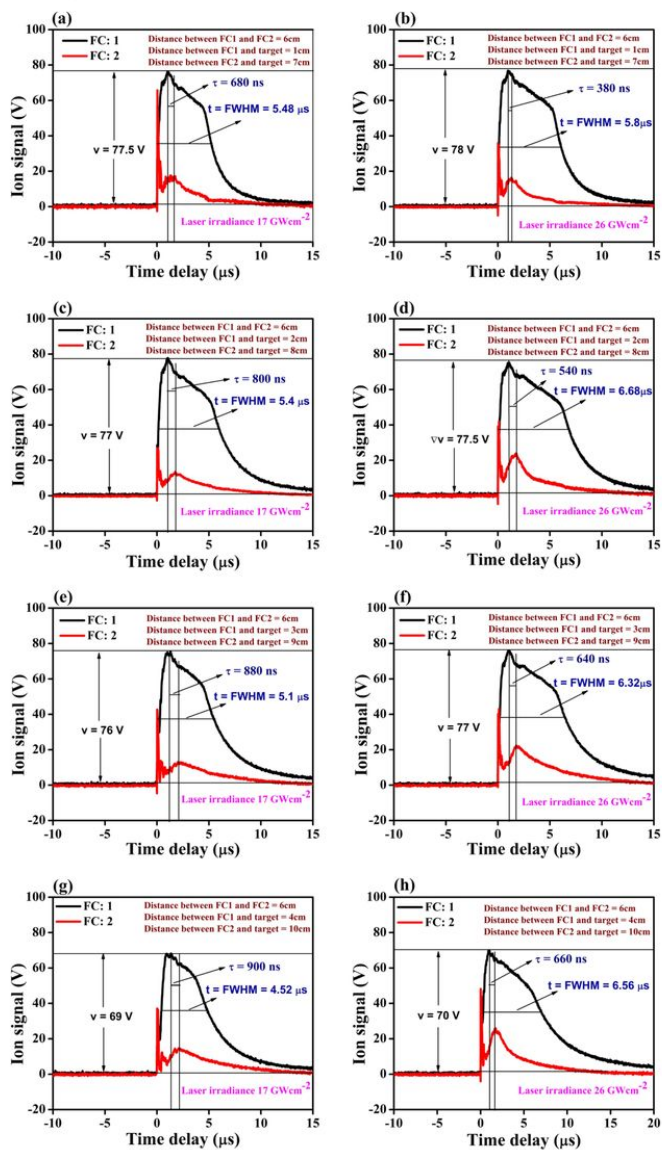


Figure 2

TOF ion signals of LIP of Zr at two selected laser irradiances at various distances of Faraday Cup (FC1) from the target i.e. (a) 1 cm, 17 GWcm⁻² (b) 1 cm, 26 GWcm⁻² (c) 2 cm, 17 GWcm⁻² (d) 2 cm, 26 GWcm⁻² (e) 3 cm, 17 GWcm⁻² (f) 3 cm, 26 GWcm⁻² (g) 4 cm, 17 GWcm⁻² and (h) 4 cm, 26 GWcm⁻².

Figure 3

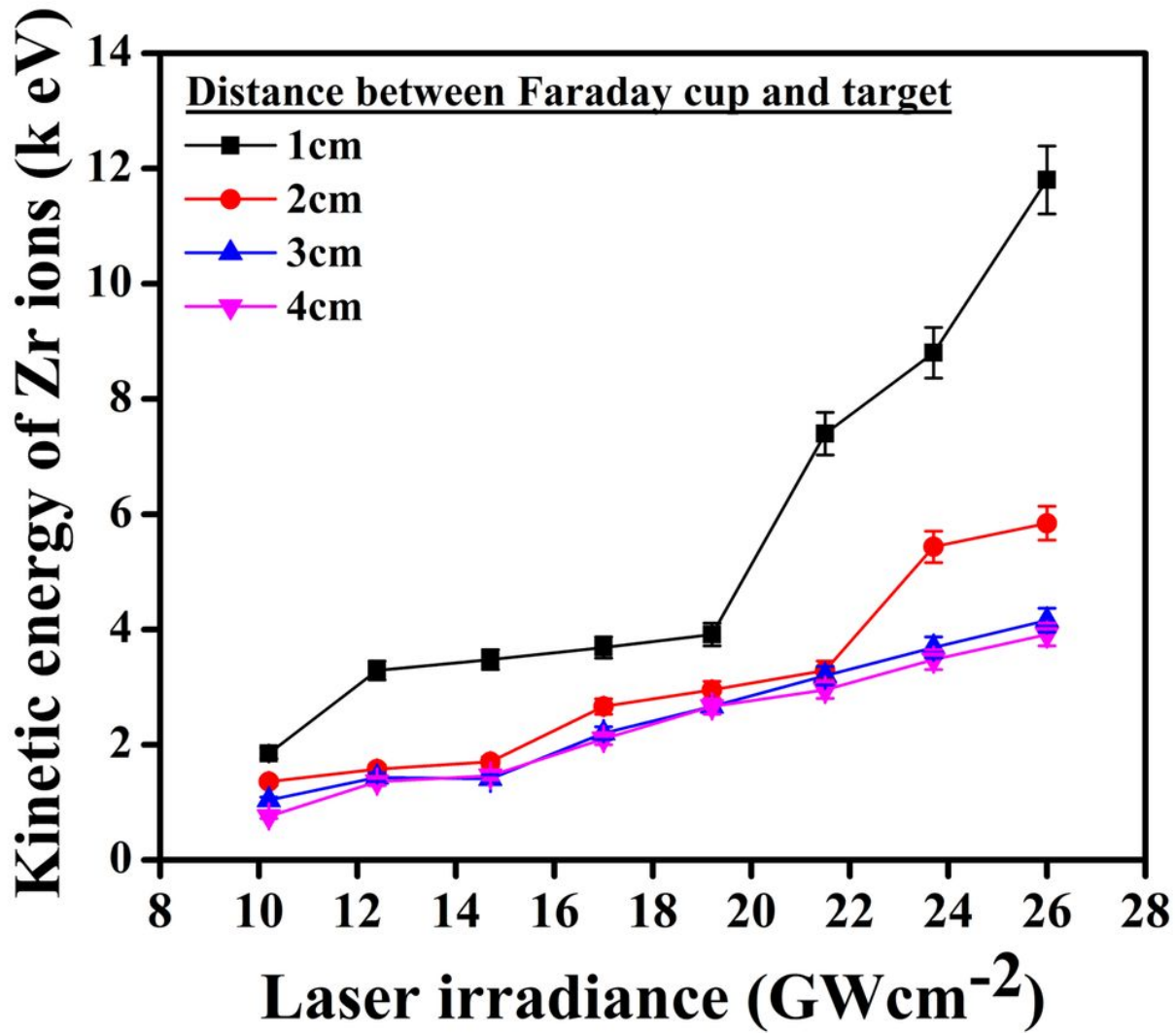


Figure 3

The kinetic energy of Zr-plasmas ions, with increasing laser irradiances at various distances of 1, 2, 3, and 4 cm of FC form Zr target.

Figure 4

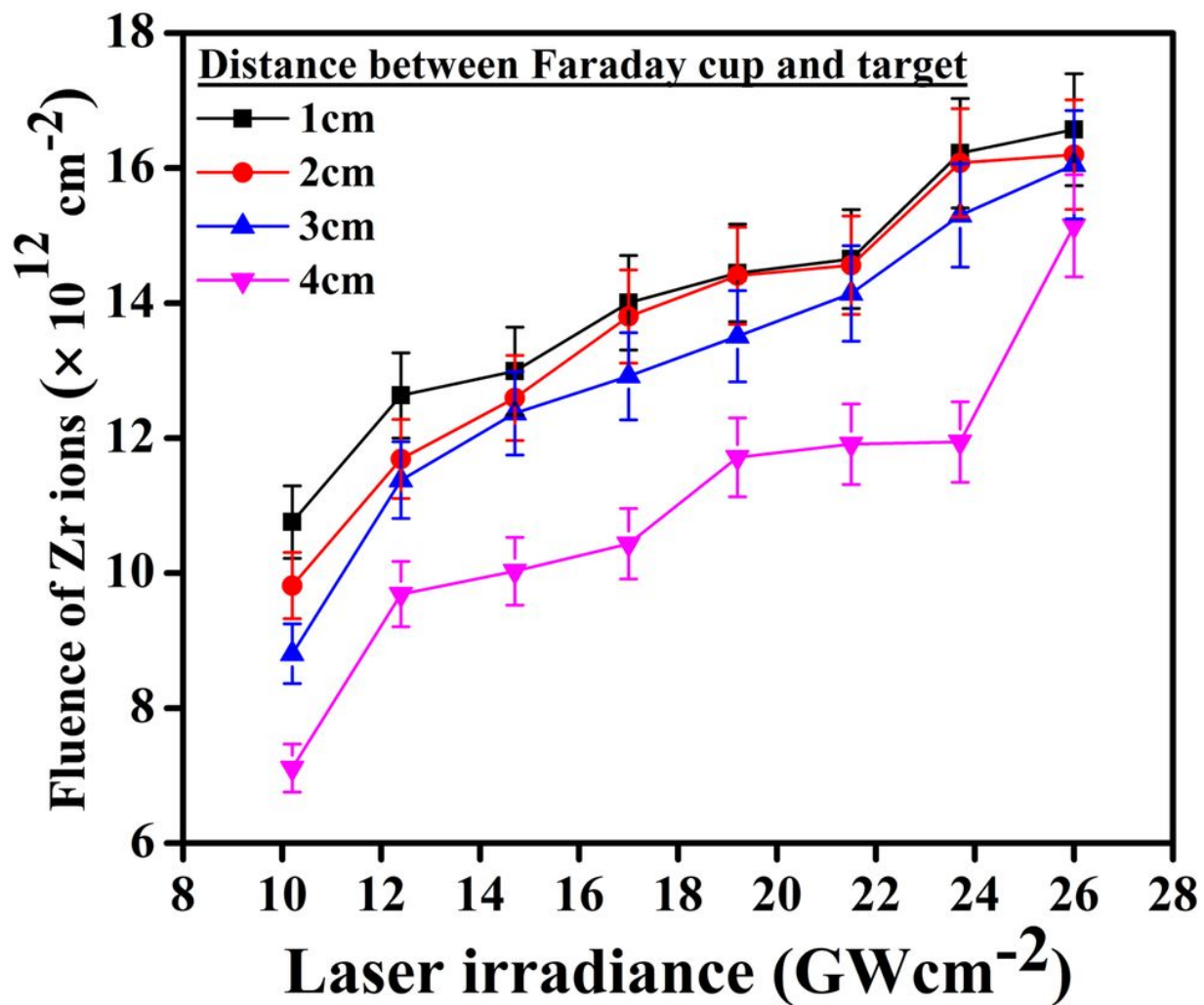


Figure 4

The ion fluence of Zr-plasmas, with increasing laser irradiances at various distances of 1, 2, 3, and 4 cm of FC form Zr target.

Figure 5

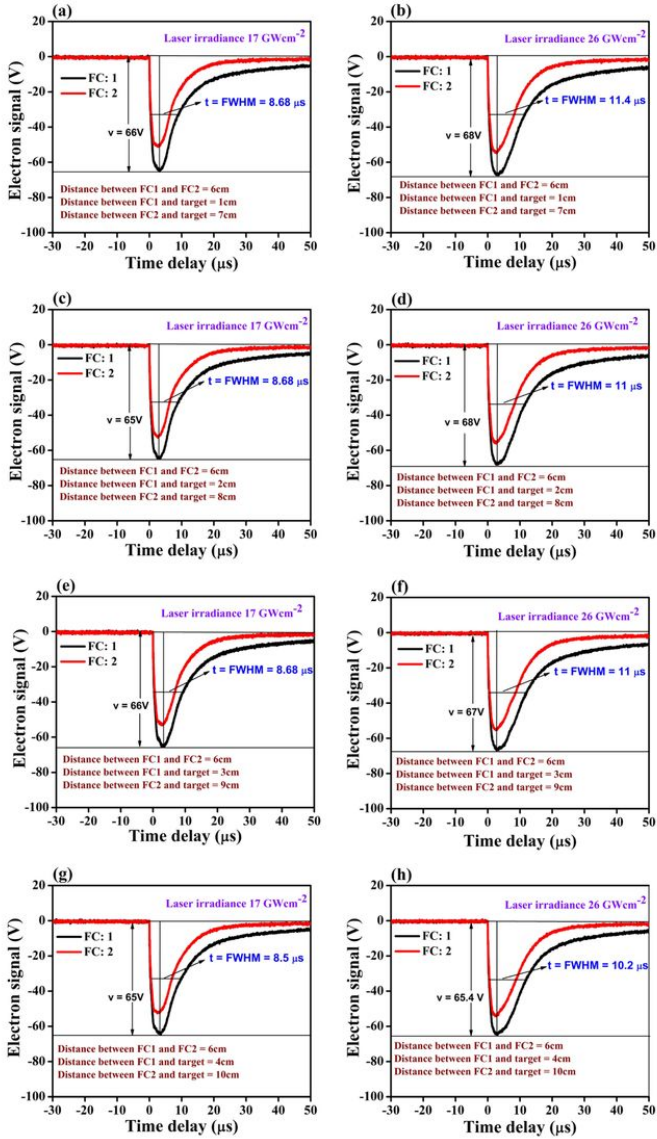


Figure 5

Simple TOF electron signals of LIP of Zr at two selected laser irradiances at various

distances of Faraday Cup (FC1) from the target i.e. (a) 1 cm, 17 GWcm^{-2} (b) 1 cm, 26 GWcm^{-2} (c) 2 cm, 17 GWcm^{-2} (d) 2 cm, 26 GWcm^{-2} (e) 3 cm, 17 GWcm^{-2} (f) 3 cm, 26 GWcm^{-2} (g) 4 cm, 17 GWcm^{-2} and (h) 4 cm, 26 GWcm^{-2} .

Figure 6

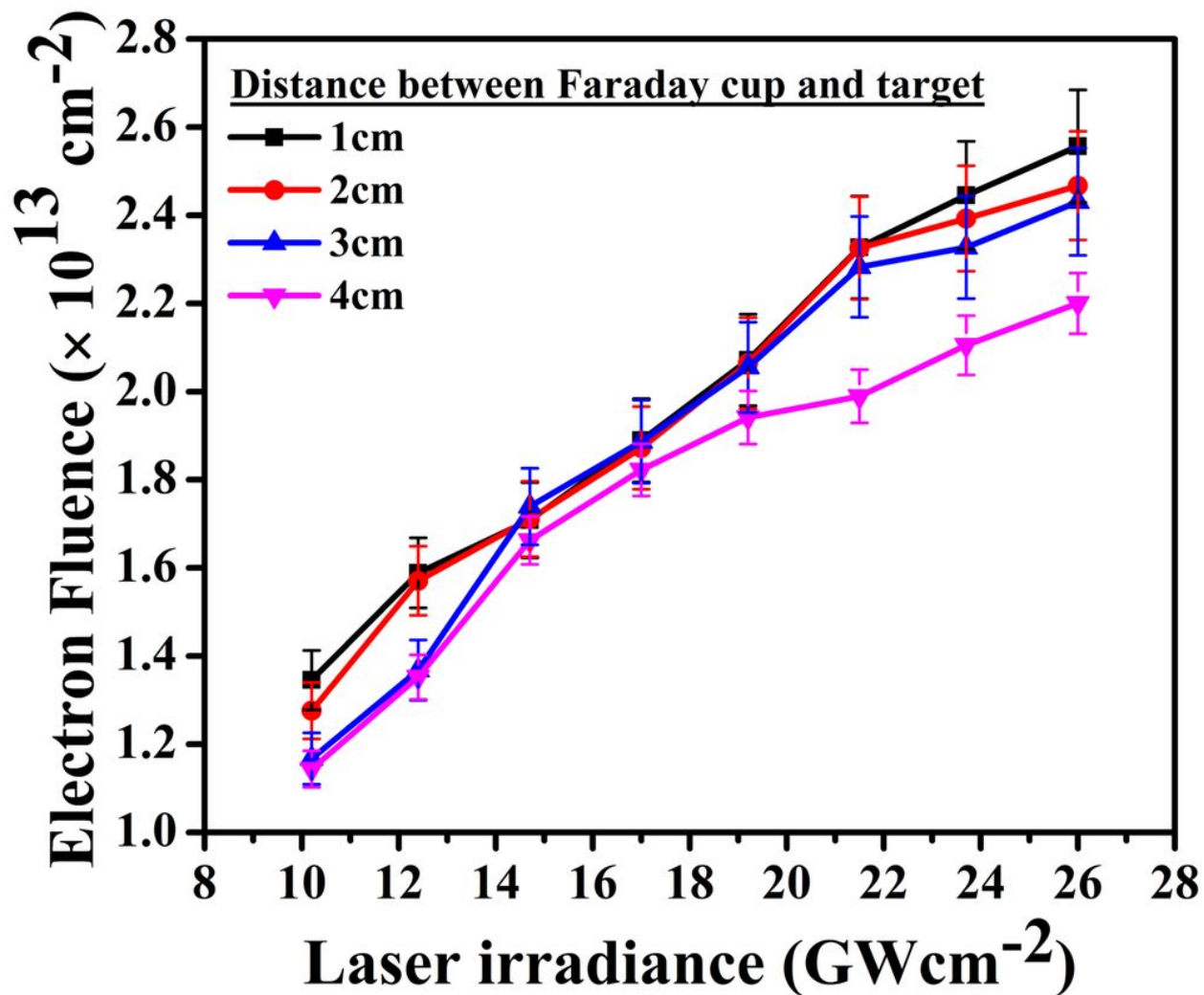


Figure 6

The electron fluence of Zr-plasmas, with increasing laser irradiances at various distances of 1, 2, 3, and 4 cm of FC form Zr target.

Figure 7

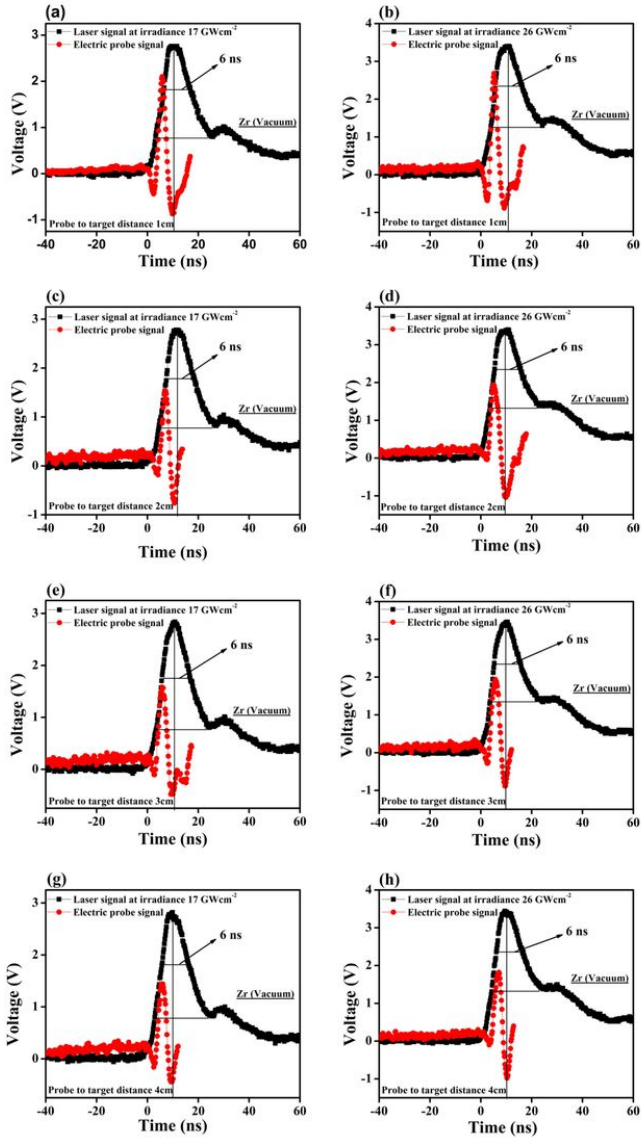


Figure 7

Temporal profiles of the SGEF signals (red trace) of Zr-plasma and the laser pulse

(black trace) at two selected laser irradiances at various distances of electric probe from the target i.e. (a) 1 cm, 17 GWcm^{-2} (b) 1 cm, 26 GWcm^{-2} (c) 2 cm, 17 GWcm^{-2} (d) 2 cm, 26 GWcm^{-2} (e) 3 cm, 17 GWcm^{-2} (f) 3cm, 26 GWcm^{-2} (g) 4 cm, 17 GWcm^{-2} and (h) 4 cm, 26 GWcm^{-2} .

Figure 8

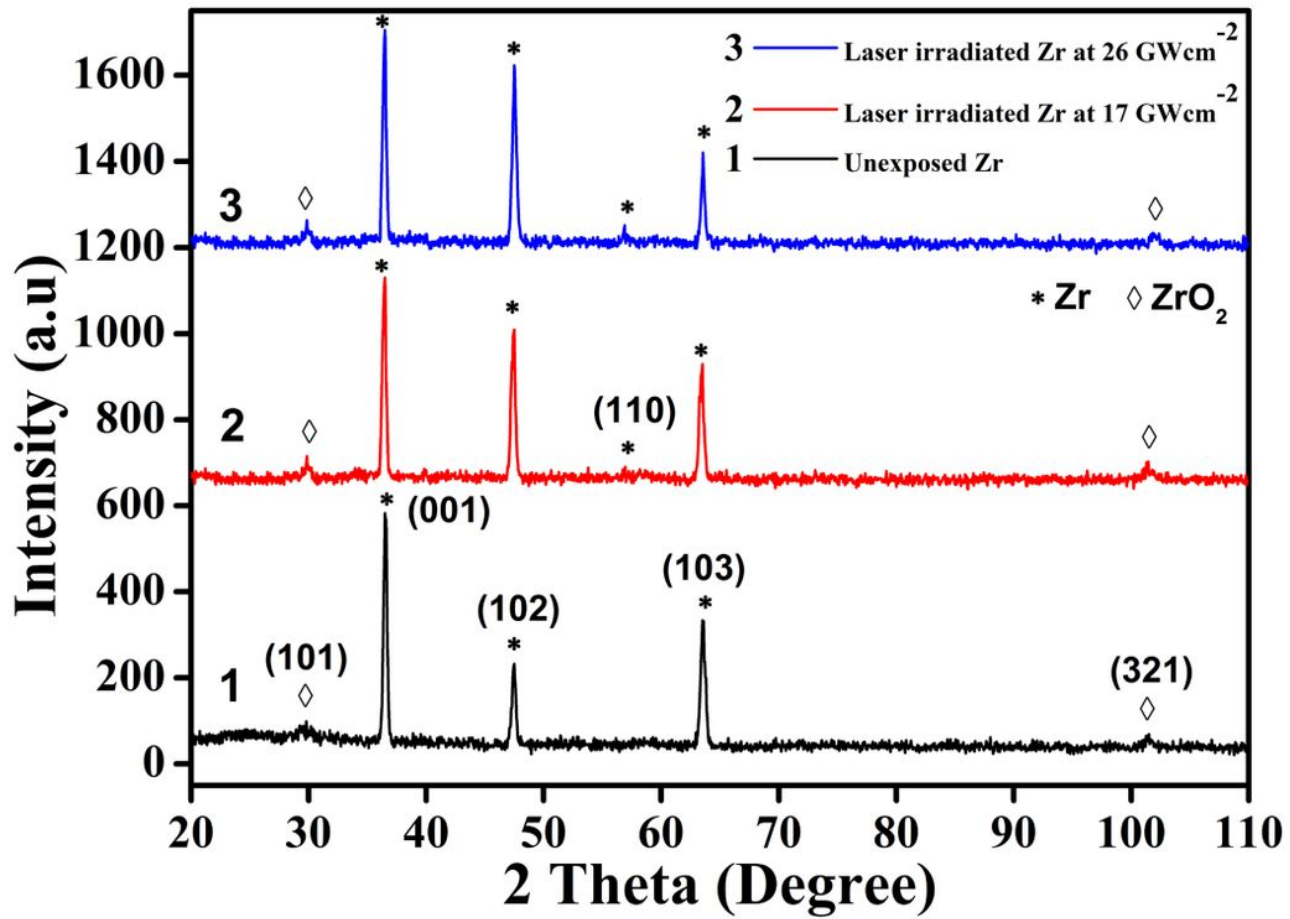


Figure 8

XRD patterns of unexposed and Nd:YAG laser irradiated Zr for two laser irradiances of 17 and 26 .

Figure 9

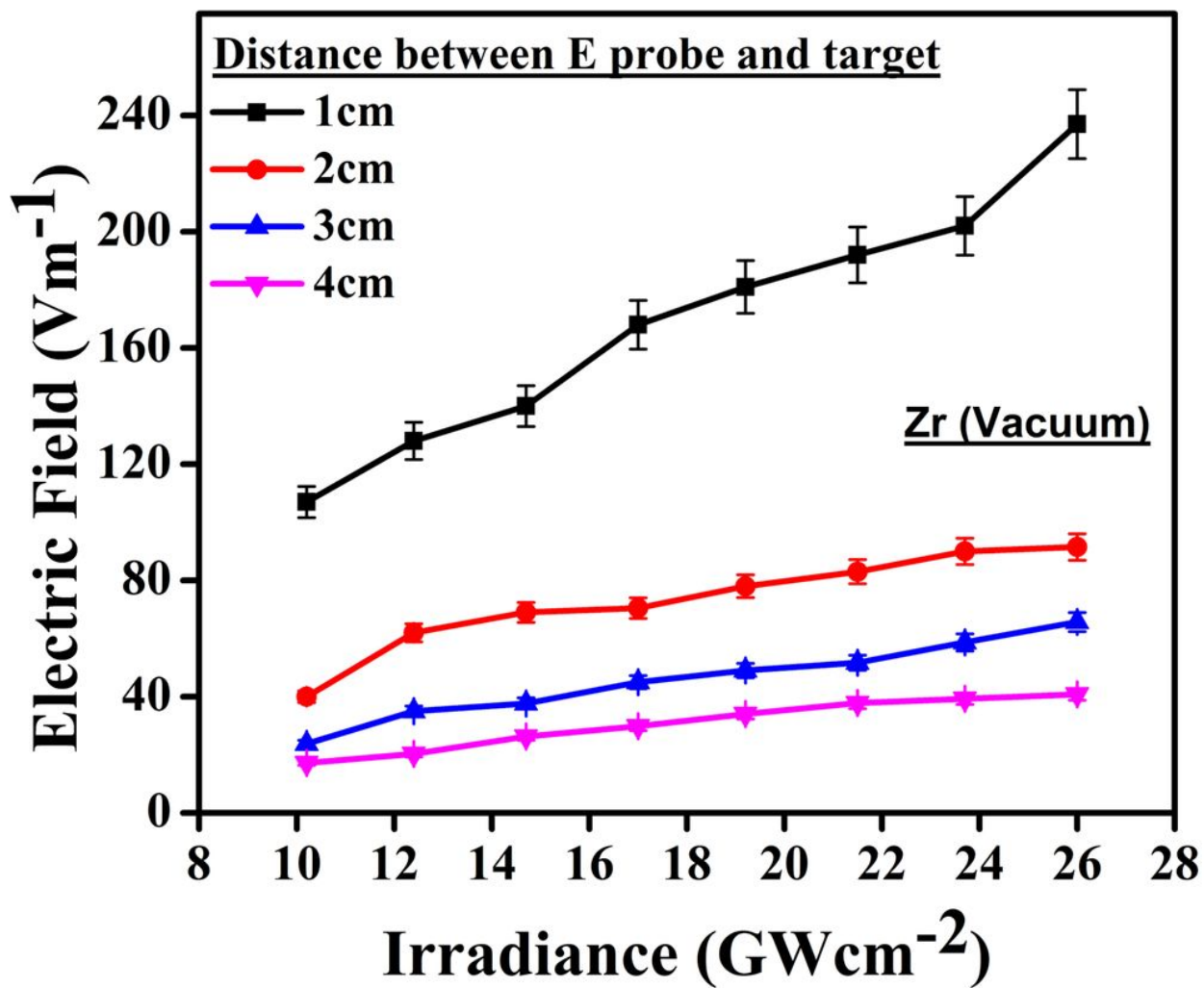


Figure 9

The SGEF of Zr-plasma with increasing the laser irradiance at different distances of 1, 2, 3, and 4 cm of electric probe from the surface of target.

Figure 10

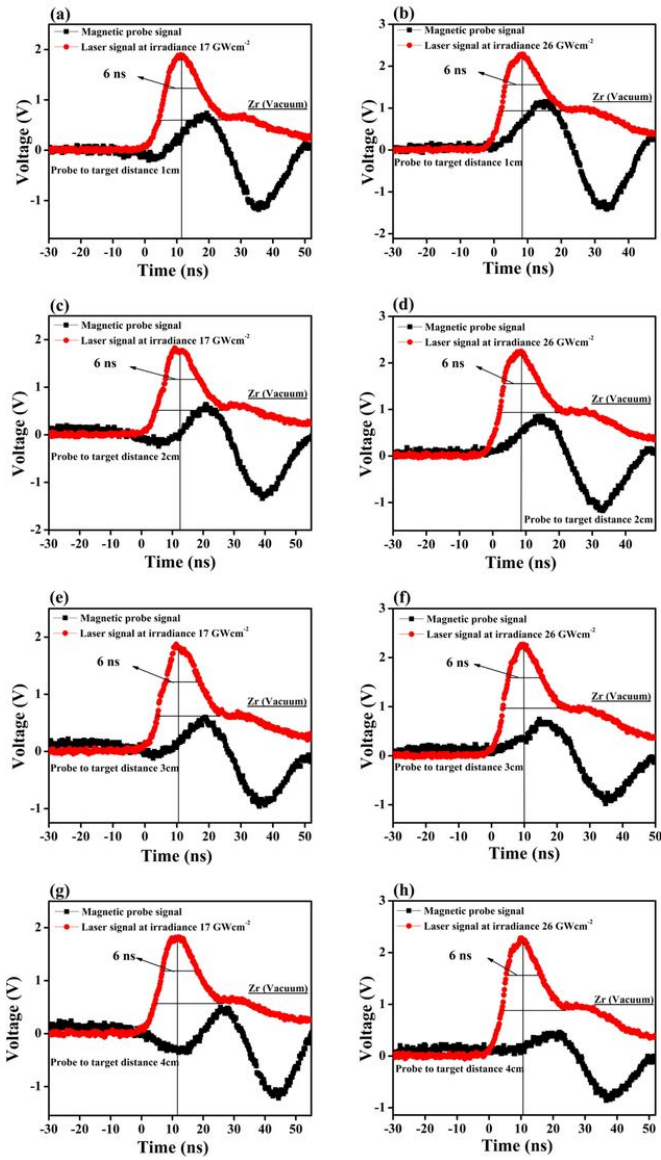


Figure 10

Temporal profiles of the magnetic probe signal (red trace) of Zr-plasma and the laser pulse (black trace) at two selected laser irradiances at various distances of magnetic probe from the target i.e. (a) 1 cm, 17 GWcm⁻² (b) 1 cm, 26 GWcm⁻² (c) 2 cm, 17 GWcm⁻² (d) 2 cm, 26 GWcm⁻² (e) 3 cm, 17 GWcm⁻² (f) 3cm, 26 GWcm⁻² (g) 4 cm, 17 GWcm⁻² and (h) 4 cm, 26 GWcm⁻².

Figure 11

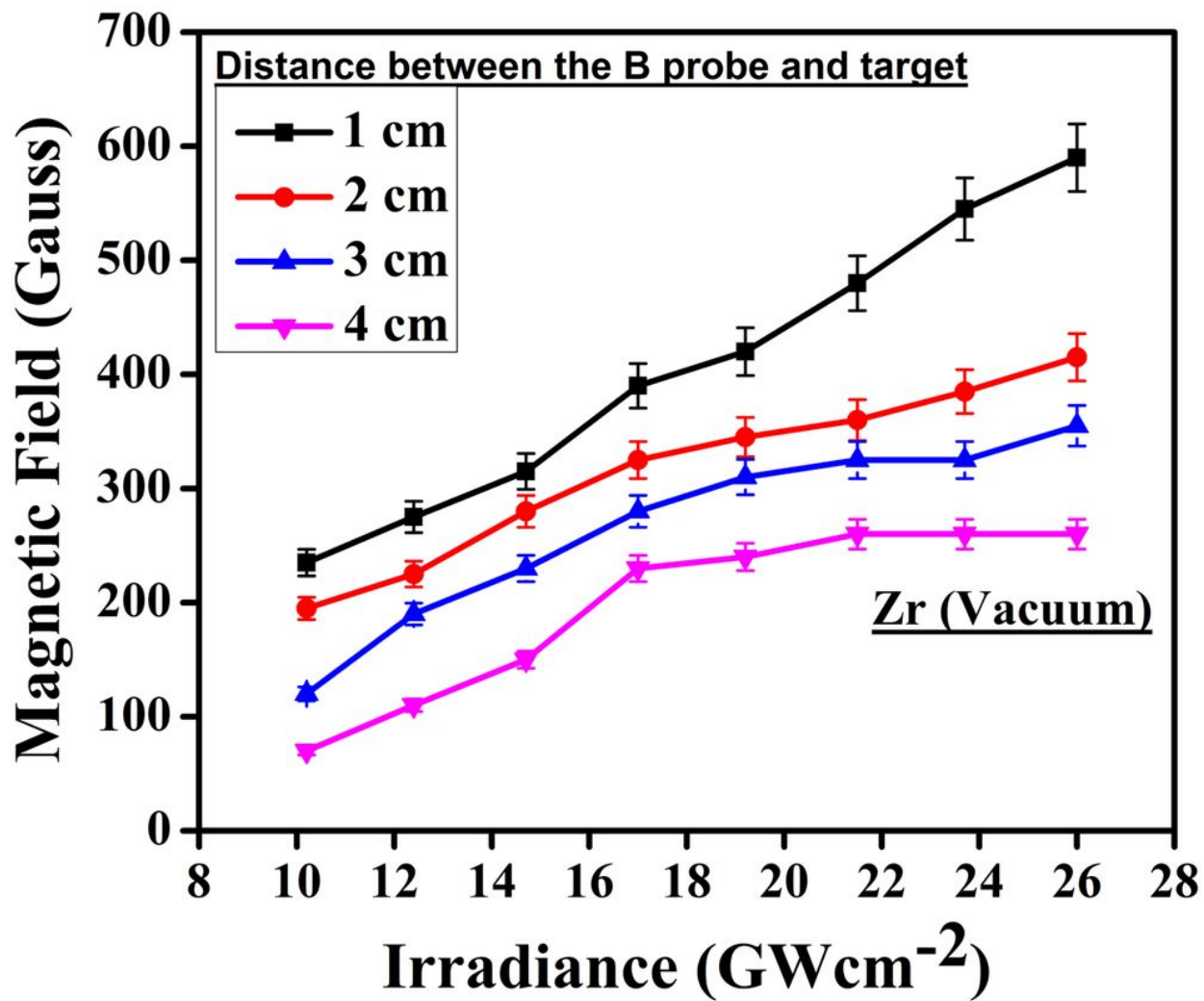


Figure 11

The SGMF of LIP of Zr with increasing the laser irradiance at different distances of 1, 2, 3, and 4 cm of magnetic probe from the target surface.

Figure 12

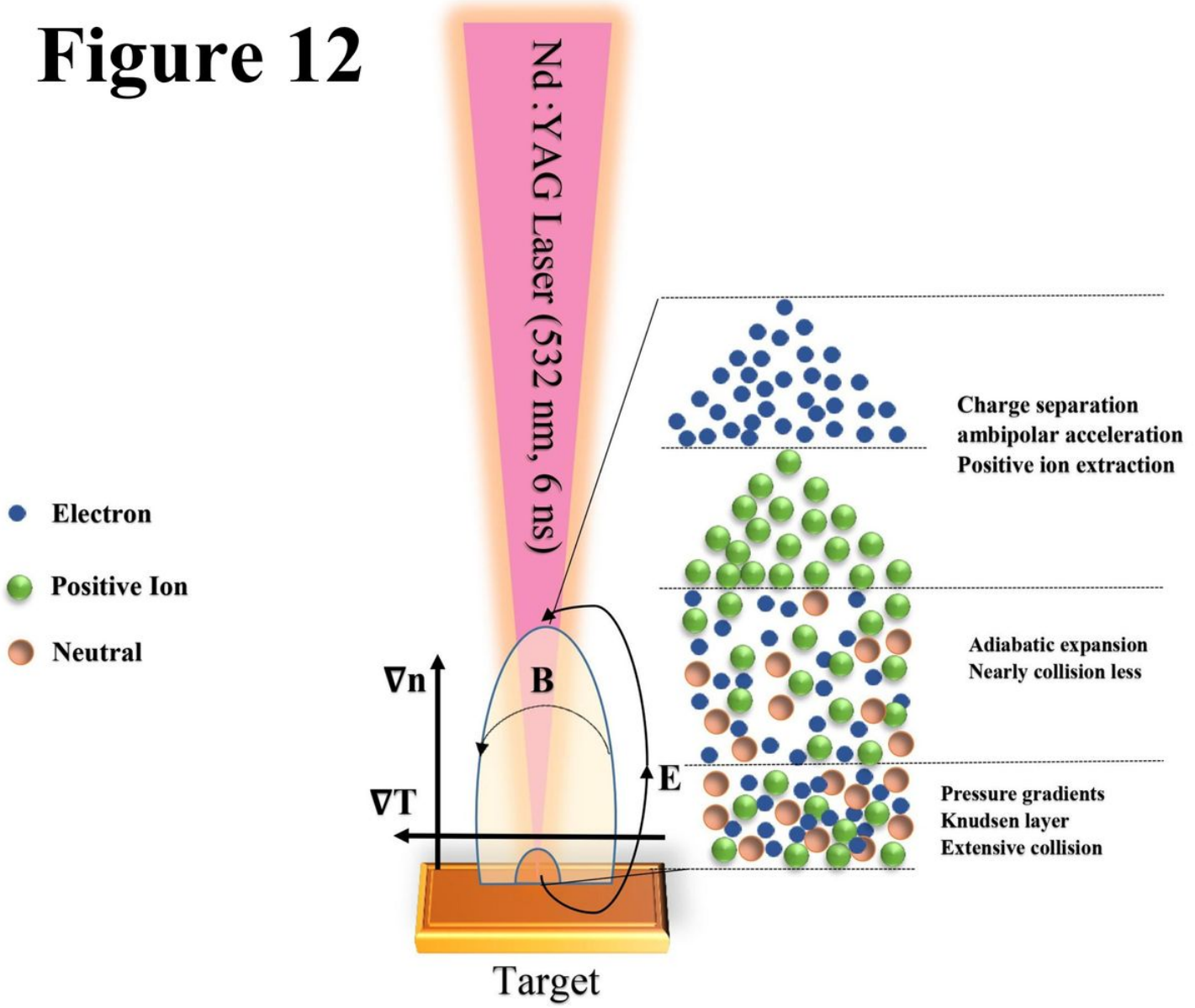


Figure 12

Schematic illustration of the separation of charge with double layer structure among fast and slow moving Zr-electrons, as well as fast and slow moving ions with ambipolar acceleration, which represents quadrupole distribution, during the LIP of Zr.

Figure 13

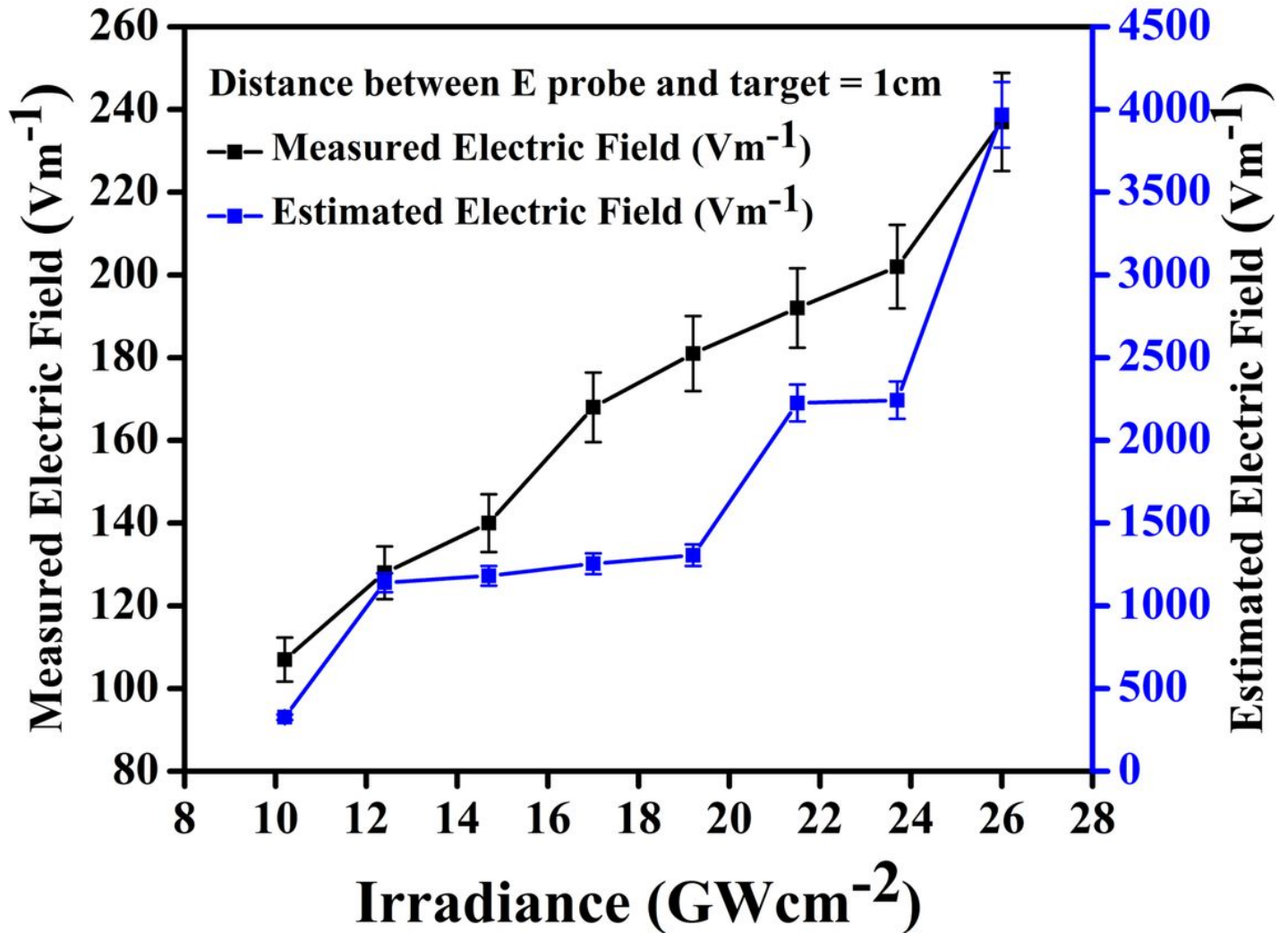


Figure 13

The direct measured (electric probe) and calculated (by density and temperature gradient) SGMF of Zr-plasma by increasing the laser irradiance at 1 cm distance from target to probe.